Journal of Materials Chemistry A

ROYAL SOCIETY OF CHEMISTRY

PAPER

View Article Online
View Journal | View Issue

Cite this: J. Mater. Chem. A, 2020, 8, 2001

Pressure-promoted irregular $CoMoP_2$ nanoparticles activated by surface reconstruction for oxygen evolution reaction electrocatalysts†

Shishuai Xu,‡[ab] Xiang Gao,‡[b] Amol Deshmukh,‡[c] Junshuang Zhou,[d] Ning Chen,[e] Wenfeng Peng,[b] Yutong Gong,[f] Zhiqiang Yao,[g] Kenneth D. Finkelstein,[h] Biao Wan,[a] Faming Gao,[c] Mingzhi Wang,*[a] Mingyang Chen*[ic] and Huiyang Gou*[b]

Developing highly ordered and conductive phosphorous-based materials and identifying their active sites are critical to improve the catalytic performance for oxygen evolution reactions (OERs). Herein, we report a template-free and rapid high-pressure synthesis protocol to fabricate irregular $CoMoP_2$ nanoparticles for OER catalysts. Pure $CoMoP_2$ electrocatalysts show a reduced overpotential of 270 mV at 10 mA cm^{-2}, improved kinetics and long-term stability. XAS, XPS and DFT calculations reveal that the reorganization induces highly active Co sites with a $Co(OH)_2$ layer on the surface, while Mo atoms regulate electronic conductivity towards OER reduction potential and maintain the structural integrity of $CoMoP_2$. This work not only provides an identified activation mechanism for bimetallic catalysts, but also highlights the high-pressure synthesis as one of the alternative approaches for developing OER catalysts.

Received 25th October 2019
Accepted 10th December 2019

DOI: 10.1039/c9ta11775j

rsc.li/materials-a

Introduction

Water oxidation associated with the conversion of electric energy into clean and renewable chemical energy is of importance in energy conversion and storage systems such as water-splitting cells, rechargeable metal–air batteries and fuel cells.[1] The oxygen evolution reaction (OER) is the anode reaction of water splitting to produce molecular oxygen during water oxidation. Due to sluggish kinetics involving the multiple proton-coupled electron transfer in OERs,[2] there is an increasing need to improve the conversion efficiency of electro-catalysts. Tremendous efforts have been devoted to exploring highly efficient and cost-effective OER electro-catalysts to replace the high-cost and scarce noble metal oxides.[3–6]

In recent years, transition metal phosphides (TMPs) have been found to be an interesting class of OER catalysts because of their earth-abundance, outstanding catalytic activity and infinite function tunability.[7] During the electrochemical process, phosphorus atoms can accommodate electrons enhancing the charge density on the phosphide surface, and phosphates that form on the surface can prompt proton-coupled electron transfers.[8] As we know, the overall OER performance is determined by the adsorption energy (ΔG_o^*) between the exposed metal active sites and O species (O*, OH* or OOH*), and ΔG_o^* is closely related to the electronic structure of transition metal atoms.[9] Therefore, compositional control of binary phosphides has been recently performed by introducing 3d-transition metals (TMs) such as ternary $Ni_{2-x}Fe_xP$, Fe-doped CoP and M(Fe/Co/Mo)-doped Ni_2P[11–13] to tailor electronic structures essentially for boosting OERs.[10]

Currently, various conventional experimental methods have been employed to realize phosphide catalysts under atmospheric pressure.[14,15] Such examples include a nano-tubular structure of Cr-doped FeNiP/NCN prepared *via* a pyrolysis-phosphide process,[16] an Ni-doped CoP_3/CC nano-needle array synthesized by a hydrothermal method followed by a phosphidation process,[17] translucent nanosheets of Fe-CoP/CoO prepared by an instantaneous method utilizing molten,[18] bicontinuous nanoporous np-$(Ni_{0.67}Fe_{0.33})_4P_5$ fabricated by electrochemical dealloying,[19] and a hierarchical flower-like CoM-P-3DHFLM (M = Ni, Mn, and Cu) derived from bottom-

[a]State Key Laboratory of Metastable Materials Science and Technology, Yanshan University, Qinhuangdao, 066004, China. E-mail: wmzw@ysu.edu.cn
[b]Center for High Pressure Science and Technology Advanced Research, Beijing, 100094, China. E-mail: huiyang.gou@gmail.com
[c]Beijing Computational Science Research Center, Beijing, 100193, China
[d]College of Environment and Chemical Engineering, Yanshan University, Qinhuangdao, 066004, China
[e]Canadian Light Source, Saskatoon, SK, CAN S7N 0X4, Canada
[f]International Center for Materials Discovery, School of Materials Science and Engineering, Northwestern Polytechnical University, Xi'an, Shanxi 710072, China
[g]School of Materials Science and Engineering, Zhengzhou University, Zhengzhou 10459, China
[h]Cornell High Energy Synchrotron Source (CHESS), Cornell University, New York 14853, USA
[i]Center for Green Innovation, School of Materials Science and Engineering, University of Science and Technology Beijing, Beijing 100083, China. E-mail: mychen@ustb.edu.cn

† Electronic supplementary information (ESI) available. See DOI: 10.1039/c9ta11775j

‡ S. Xu, X. Gao and A. Deshmukh are contributed equally.

up MOF-intermediated synthesis.[20] Nevertheless, the general synthetic strategies suffer from complex procedures, imprecise control, poor crystallinity and phase separation leading to difficulties in performance optimization and mechanism understanding. Thus, it is of great significance to develop a facile synthesis method to obtain a pure, homogeneous and high-activity phosphide catalyst.

High pressure (HP), as an additional thermodynamic parameter to conventional synthesis, is an efficient and clean approach for the rapid realization of solid-state compounds not accessible at ambient pressure.[21–23] Extensive progress made in high-pressure chemistry has enabled the understanding of chemical reactions of inorganic compounds for OER catalysts, such as Co-doped Fe_3C@CNOs, perovskite $CaCu_3Fe_4O_{12}$ and $Ba_{0.5}Sr_{0.5}Co_{0.8}Fe_{0.2}O_{3-\delta}$.[24–26]

High pressure has advantages of clean and simple procedure and rapid reaction that effectively surmount the deficiency of conventional synthetic routes.[27] Herein, we report the synthesis of $CoMoP_2$ irregular nanoparticles by a rapid high-pressure annealing approach. $CoMoP_2$ exhibits particle-like shapes containing irregular nanoparticles and have remarkable catalytic activity and long-term stability. Experimental results suggest that the surface reconstruction of homogeneous $CoMoP_2$ produces a layer of Co hydroxide that boosts the OER activity. The DFT reveals the roles of Co, Mo and hydroxide species for the enhanced OER of $CoMoP_2$. The present results highlight the great significance of exploring homogeneous structures of multi-metal phosphides for catalysts, and accurately identifying the active sites without complex structure interference.

Results and discussion

A rapid high-pressure process is performed for the preparation of crystalline $CoMoP_2$ followed by ball-milling treatment (Scheme 1). First, all reagents of Co, Mo and P were weighed by molar ratio (1 : 1 : 2), well-mixed and then heated at 1500 °C for 5 min under 5 GPa to form bulk $CoMoP_2$. Finally, as-synthesized $CoMoP_2$ is ball-milled to a fine powder. Fig. S1a† shows that $CoMoP_2$ can be indexed with the hexagonal phase (space group: $P6_3/mmc$, JCPDS# 33-0428),[28] and the diffraction peaks at $2\theta = 15.8°$, 31.4°, 45.4° and 55.7° are corresponding to the (002), (100), (104) and (110) crystal planes of hexagonal $CoMoP_2$. The structural parameters of $CoMoP_2$ were obtained by the Rietveld refinement (Fig. 1a) with lattice parameters of $a = b = 3.296$ Å, $c = 11.223$ Å, indicating the successful synthesis of a single-phase $CoMoP_2$. Meanwhile, MoP_2 and CoP_2 were also synthesized to make comparison under the same high-pressure condition. The diffraction peaks are in accordance with the orthorhombic structure (JCPDS# 76-2363) and the monoclinic structure (JCPDS# 77-0263) shown in Fig. S1b and c.† Nevertheless, when synthesized at ambient pressure, Fig. S1d† shows the multiphase feature, not a single phase (Fig. 1a and S1a†).

Scanning electron microscopic (SEM) images reveal that the as-prepared $CoMoP_2$ nanoparticles have spherical shapes with grain sizes ranging from tens to hundreds of nano-meters (Fig. 1b). In addition, the spherical structure of $CoMoP_2$ consists of irregular nanoparticles with very rough surface shown in Fig. S2a.† Transmission electron microscopic (TEM) images of $CoMoP_2$ further confirm that a large number of nanoparticles with an average diameter of about 50 nm are stacked randomly to form spheroidal clusters (Fig. 1c and S3a†). The nanoparticles with rough surfaces can ensure sufficient contact between the catalyst and the electrolyte facilitating

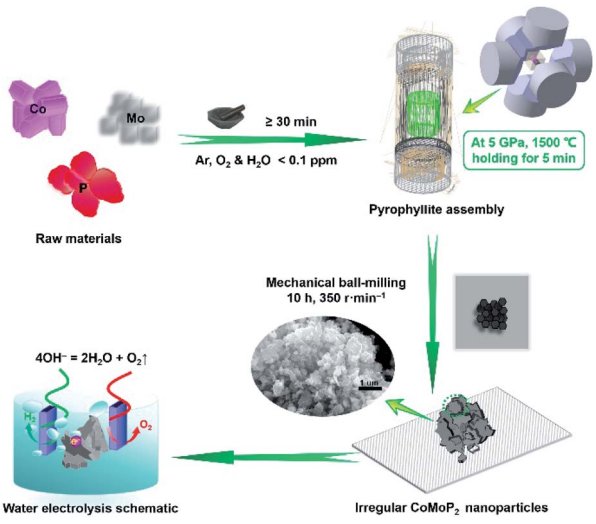

Scheme 1 Schematic of the synthesis process of irregular $CoMoP_2$ nanoparticles, including bulk sample preparation by HP and mechanical ball-milling process.

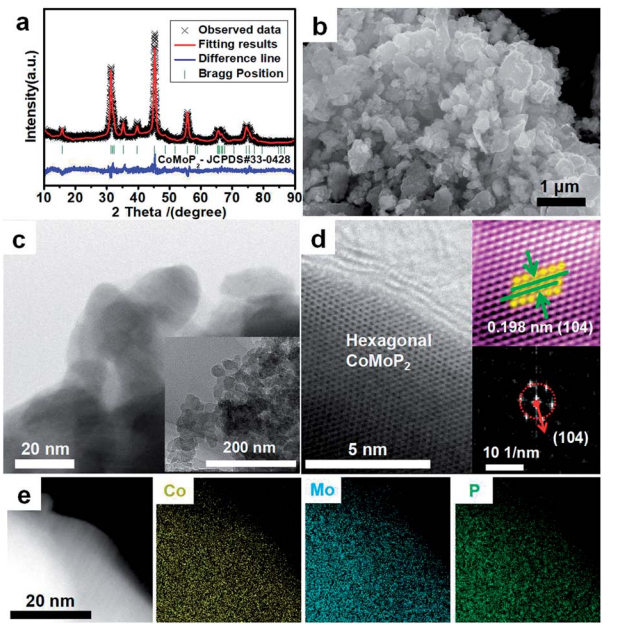

Fig. 1 Characterization of bimetallic phosphides ($CoMoP_2$). (a) Rietveld refinement XRD patterns of $CoMoP_2$ nanoparticles. (b) SEM image. (c) Bright-field TEM image. (d) High-resolution TEM image, with the inset showing the corresponding fast-Fourier transform diffraction pattern of the red circle area. (e) High-angle annular dark-field (HAADF) image and the corresponding elemental maps of Co, Mo and P atoms.

electron transfer. High-resolution TEM (HRTEM) images illustrate $CoMoP_2$ with a clear crystal lattice fringe in Fig. 1d and S3b.† The interlamellar spacings of 0.198 nm, 0.274 nm and 0.250 nm are assigned to the (104), (101) and (102) planes of $CoMoP_2$. The corresponding inverse Fourier transform of the red circle area shows a typical hexagonal symmetry (inset of Fig. 1d), confirming high crystallinity. The high-angle annular dark-field (HAADF) and element mappings demonstrate that Co, Mo and P elements are distributed homogeneously throughout the whole particles (Fig. 1e, S2b and c†), having the atomic ratio of 1 : 1 : 2, shown in Fig. S3c and Table S1.† Comparative samples of MoP_2 and CoP_2 also show the irregular agglomerates with rough edges. Co (Mo) and P atoms are homogeneously distributed in an atomic ratio close to 1 : 2 (Fig. S4 and Table S1†).

The catalytic activity of $CoMoP_2$ towards OERs is investigated in 1 M KOH. The catalysts went through about 5 cyclic voltammetry (CV) cycles until a stable linear sweep voltammetry (LSV) curve was obtained at 50 mV s^{-1}. Fig. 2a shows that $CoMoP_2$ has a lower overpotential of 270 mV to achieve a current density of 10 mA cm^{-2} ($\eta_{10} = 270$ mV) compared with commercial RuO_2/C (344 mV). Fig. 2b indicates that $CoMoP_2$ exhibits outstanding performance compared to $MnCoPO_x$ (320 mV),[29] FeP_x/FeNC/NPC (330 mV),[30] Co_2P/Co foil (319 mV),[31] $Fe_{1.1}Mn_{0.9}P$ (350 mV) and $Co_{0.6}Fe_{0.4}P$ (300 mV),[32,33] and other reported catalysts are listed in Table S2.† In order to examine the OER kinetic activity, Tafel plots are given in Fig. 2c.[34,35] The as-prepared $CoMoP_2$ catalyst demonstrates a smaller Tafel slope of 51 mV dec^{-1} than those of CoP_2 (95 mV dec^{-1}), MoP_2 (75 mV dec^{-1}) and RuO_2/C (61 mV dec^{-1}), implying its rapid rate of OERs. In addition, electrical impedance spectroscopy (EIS) was performed to evaluate the electron transport performance (Fig. S5a†).[36] The charge-transfer resistance (R_{ct}) follows the order of $CoMoP_2$ (1.8 ohm) > MoP_2 (3.3 ohm) > CoP_2 (5.1 ohm). The $CoMoP_2$ has the lowest charge transfer resistance among all samples. The results further indicate that the electronic structure tuning could greatly accelerate the electron transfer at the interface during the OER process.

To assess electrochemically active surface area,[37–39] electrochemical double-layer capacitances (C_{dl}) were measured by the CV method (Fig. 2d and S5b–e†). The as-prepared $CoMoP_2$ presents a great C_{dl} value (11.2 mF cm^{-2}), compared to those of RuO_2/C (6.8 mF cm^{-2}), MoP_2 (1.5 mF cm^{-2}), and CoP_2 (1.1 mF cm^{-2}), revealing the enhancement of anion exchangeability between active sites and electrolyte. Fig. S5f† shows high faradaic efficiency, suggesting the reaction attributed to OERs. The TOF of $CoMoP_2$ (2.12×10^{-2} s^{-1}) is higher than those of RuO_2/C (0.39×10^{-2} s^{-1}), MoP_2 (0.17×10^{-2} s^{-1}) and CoP_2 (0.06×10^{-2} s^{-1}) (Fig. 2e), while the normalized LSV curves by C_{dl} exhibit superior OER activity in Fig. S6,† indicating the highly intrinsic OER activity.[40] In addition, the great stability is also critical for energy conversion and storage devices.[41] After 6000 cycles, the polarization curve of $CoMoP_2$ exhibits only slight OER current degradation with an electrode at 100 mV s^{-1} compared with the first curve (Fig. 2f), while the *i*–*t* curve also shows that the catalytic current density is maintained around 10 mA cm^{-2} over 20 h of testing in alkaline solutions (inset image in Fig. 2f), suggesting its superior catalytic durability and structural stability.

After OER testing, the $CoMoP_2$ catalyst maintains the original crystal symmetry (Fig. 3a), but new diffraction peaks at $2\theta = 19.2°$, 38.0° and 51.6° appear, which match well with the crystalline phase of $Co(OH)_2$ (JCPDS# 51-1731),[42,43] implying that the surface of $CoMoP_2$ underwent structural reorganization

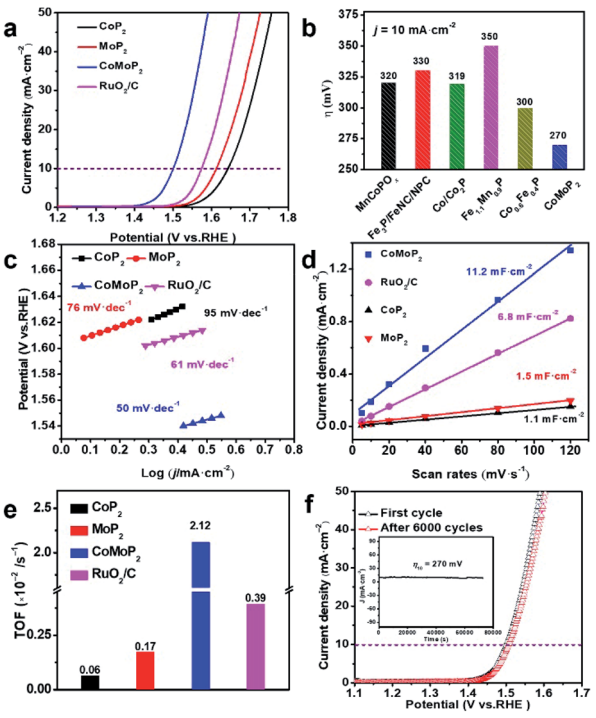

Fig. 2 Performance of different catalysts in 1 M KOH aqueous electrolyte. (a) OER polarization curve without iR correction, (b) comparison of the overpotentials at 10 mA cm^{-2} between this catalyst and other reported metal phosphides and (c) Tafel plots. (d) Electrochemical double-layer capacitance at different scan rates, and corresponding (e) turnover frequency (TOF) of $CoMoP_2$, MoP_2 and MoP_2. (f) Polarization curves for $CoMoP_2$ before and after 6000 cycles. Inset: amperometric *i*–*t* curve was obtained at a constant current density of 10 mA cm^{-2} over 20 h.

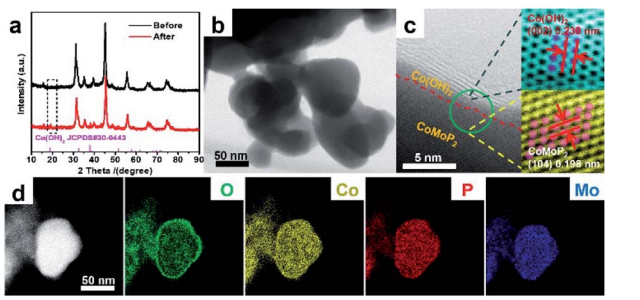

Fig. 3 (a) XRD patterns of $CoMoP_2$ samples before and after electrolysis for 20 h. (b) TEM image and (c) ABF-STEM image with magnified images showing atom arrangement at the boundary region. (d) Bright-field TEM image with the corresponding elemental mapping of $CoMoP_2$ after OERs.

to form $Co(OH)_2$. The SEM images show that the morphology of $CoMoP_2$ has a slight change after the OER process (Fig. 3b and S7a†), but the core–shell structure is found with a shell thickness of about 4 nm (Fig. S7b†). The HRTEM image shows the interplanar spacings of the core and shell, which are 0.198 nm and 0.230 nm, in accordance with the (104) and (002) planes of $CoMoP_2$ and $Co(OH)_2$ (Fig. 3c), respectively. The EDS mappings show that Co, Mo and P elements are uniformly distributed in all particles, while the O element is mainly concentrated on the surface of the particle (Fig. 3d). The results indicate that the reorganizations induce the formation of cobalt hydroxides on the surface of $CoMoP_2$, indicating that the surface Co atoms have high activity.[44]

The surface valence states and chemical compositions of $CoMoP_2$, CoP_2 and MoP_2 catalysts were investigated by X-ray photoelectron spectroscopy (XPS). The XPS survey (Fig. S8a†) demonstrates that the surface of $CoMoP_2$ contains Co, Mo, P and O elements, and the existence of O is due to air exposure. After OERs, the atomic ratio of Co : Mo : P : O on the surface has changed to 5.47 : 4.28 : 10.55 : 79.7, compared with those of 3.03 : 8.20 : 17.99 : 70.78 for $CoMoP_2$ before the OER. The contents of Co and O increase, accompanied by a decrease in Mo 3d and P 2p contents (Fig. S8a†), consistent with a $Co(OH)_2$ shell generated for covering up the signals on the surface. In the high-resolution XPS spectrum of Co 2p (Fig. 4a), Co $2p_{3/2}$ located at 778.18 eV and 792.83 eV are assigned to Co–P (Co^0),[45] and the peaks located at 780.93 eV and 797.4 eV are attributed to the oxidized Co species (Co^{2+}).[18] Compared with CoP_2, the binding energy (BE) peak of $CoMoP_2$ before at 778.18 eV (Co^0, red line) has a relatively lower intensity, and the BE peak at 780.93 eV (Co^{2+}) is positively shifted to 781.74 eV (green line) in Fig. 4a. Meanwhile, the area ratio of 781.74/778.18 eV (abbreviated as Co^{2+}/Co^0) for $CoMoP_2$ before increases significantly from 1.01 to 6.33 compared with CoP_2, illustrating that surface Co atoms have a high oxidation state. Similarly, the BE peak at 227.57 eV (Mo–P, Mo^0), 228.77 (Mo $3d_{5/2}$) and 231.2 eV (Mo $3d_{3/2}$) in the Mo 3d region are assigned to $Mo^{\delta+}$ ($0 \leq \delta < 4$),[46] while other doublets at 232.5 (Mo^{6+}, $3d_{5/2}$) and 235.1 eV (Mo^{6+}, $3d_{3/2}$) (Fig. 4b) are ascribed to the oxidized MoO_x species.[47] The area ratio of $Mo^{\delta+}$ ($0 < \delta < 4$)/Mo^0 increases from 0.56 to 1.68, while the $Mo^{6+}/Mo^{\delta+}$ ($0 < \delta < 4$) ratio drops from 3.25 to 0.49 compared with MoP_2, suggesting the strong interaction between Co and Mo atoms in $CoMoP_2$.[48,49] After OERs, BE at 235.1 eV (Mo^{6+}) for $CoMoP_2$ (after OERs) is positively shifted and the ratio of $Mo^{6+}/Mo^{\delta+}$ increases significantly, suggesting a higher valence state of the Mo atom on the surface (Fig. 4b). Meanwhile, the BE peak at 778.18 eV (Co–P) disappeared and a large amount of Co^{2+} was detected on the surface compared with that before the OER (Fig. 4a), confirming that Co atoms or cobalt oxides serve as active sites on the surface. Interestingly, the electronic structure of Co is significantly affected by the strong interaction between Co and Mo atoms, which induces a large number of Co^{2+} rather than Co^{3+} on the surface, which is beneficial for the generation of intermediates ($Co(OH)_2$), facilitating the OER process.

In Fig. S8b,† O 1s spectra can be deconvolved into two bands, corresponding to O–metal bonds (531.56 eV) and H_2O (533.00 eV).[50] After the OER, the peak at 531.56 eV of $CoMoP_2$ exhibits a prominent peak assigned to the O metal in Fig. S8c,† which is related to high valence of Co active sites,[43,51] resulting in its superior electrocatalysis performance. The XPS spectra of P 2p are shown in Fig. S8b,† and the peaks at 133.71 eV and 134.45 eV are assigned to phosphate (P–O).[52–54] The peaks at 129.15 eV and 129.94 eV are found to be Co–P and Mo–P, respectively.[55] Clearly, all samples show the signals of P–O on the surfaces and the peaks for P $2p_{1/2}$ in $CoMoP_2$ are shifted toward the lower BE peak compared with the ones of CoP_2 and MoP_2. The phosphates produced can serve as proton transport mediators at the catalyst surface,[11,12] which are beneficial for the OER process.

X-ray absorption fine structure (XAFS) spectra of Co K-edge were recorded for $CoMoP_2$ (Fig. 4c and d). The presence of pre-edge peaks for $CoMoP_2$ both before and after OERs are similar to Co foil (Fig. 4c), indicating the metallic nature of Co in $CoMoP_2$ catalysts.[56] After the OER, the pre-edge peak becomes weaker due to the presence of intermediates (O, OH, and OOH) from the OER process, and the X-ray absorption near-edge structure (XANES) of Co K-edge is positively shifted to higher energies (Fig. S8d†), suggesting Co–O species (Co^{2+}, $Co(OH)_2$) on the surface. In order to precisely determine the valence state of $CoMoP_2$, the absorption energy (E_0, determined from the first peak in the derivative) of Co foil was set at 7709.1 eV. $CoMoP_2$ before the OER has a high absorption energy (E_0 = 7715.74 eV), confirming that $CoMoP_2$ before the OER has a high valence state for Co atoms. Meanwhile, the absorption energy of $CoMoP_2$ after the OER (E_0 = 7716.14 eV) is similar to those of CoO (E_0 = 7716.52 eV),[57] suggesting that the oxidation state of Co is close to Co^{2+}, which could be attributed to the formation of $Co(OH)_2$ on the surface, consistent with the above-mentioned XRD and XPS results. Moreover, the main peak is located between that of CoO and Co_2O_3, suggesting a similar coordination environment (Co oxides) for Co atoms on the $CoMoP_2$ (after the OER) surface.[58] The Fourier-transformed k^3-

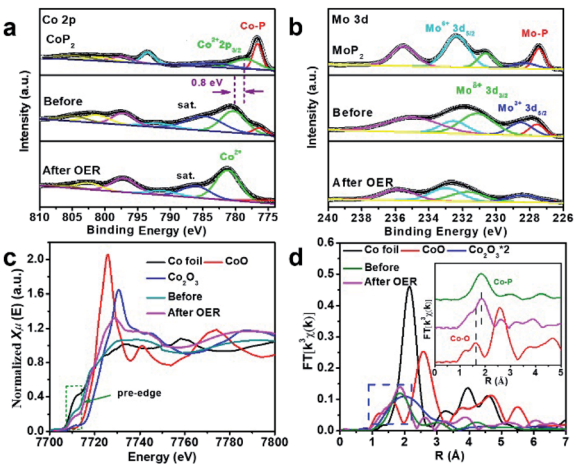

Fig. 4 Characterizations of CoP_2, MoP_2, and $CoMoP_2$ before and after the OER. High-resolution XPS spectra of (a) Co 2p and (b) Mo 3d. "Sat." indicates satellite peaks. (c) XANES spectra and (d) magnitude of FT-EXAFS spectra with a magnified inset image of Co foil, CoO, Co_2O_3, and $CoMoP_2$ before and after the OER at Co K-edges.

weighted extended X-ray absorption fine structure (FT-EXAFS) spectra at Co K-edges for $CoMoP_2$ are also displayed in Fig. 4d. The FT-EXAFS spectra of $CoMoP_2$ (before and after) show a prominent peak at 1.7 Å (Fig. 4d), attributed to the first coordination the Co–P shell,[59] indicating that $CoMoP_2$ still maintains its crystalline structure with great stability. In addition, a small Co–O peak appears close to the main peak of CoO (inset of Fig. 4d), related to the $Co(OH)_2$ shell on the surface. The EXAFS fittings were processed using $CoMoP_2$ ($P6_3/mmc$) and modified $CoMoP_2$–$Co(OH)_2$ structure models in Table S3, Fig. S8e and f.†

The fitting results show that the Co–P1 and Co–Mo1 paths (R) are 2.26 and 2.82 Å for $CoMoP_2$ before, matching well with that of the theoretical value of $CoMoP_2$ (2.27 and 2.83 Å) (Table S3†).[60] The Co–P1 path after the OER is 2.24 Å close to $CoMoP_2$ before confirming the stability structure of $CoMoP_2$. Additionally, Co–O paths are added leading to a better fitting data, confirming that a part of Co on the surface has been transformed into oxidized Co species ($Co(OH)_2$) as indicated by the XNFS analysis. The sum of average coordination number (Co–O1 and Co–P1 paths) for $CoMoP_2$ after the OER is the same as that of Co–P1 paths for $CoMoP_2$ before the OER, shown in Table S3,† and the Co–Mo1 paths (3.07 Å) for $CoMoP_2$ after the OER is longer than that before the OER (2.82 Å), which is affected by Co–O (1.90 Å) in Table S3.† Therefore, the X-ray absorption analysis shows that the Co atom in $CoMoP_2$ has a higher oxidation state as active sites formed $Co(OH)_2$ shell on the surface during the OER, while the core structure of $CoMoP_2$ remains unchanged explaining the catalytic stability.

To understand the OER performance, the density of states (DOS) of $CoMoP_2$, CoP_2 and MoP_2 were calculated to uncover the electronic structure (Fig. S9†). $CoMoP_2$ has a conductive electronic structure (DOS of 1.7 states per eV at Fermi level) (Fig. S9a†), while both CoP_2 and MoP_2 have semi-conductive behaviors, exhibiting relatively weaker electronic conductivities (Fig. S9b and c†). The OER over $CoMoP_2$ and comparable systems were investigated using the density functional theory (DFT) within the Perdew–Burke–Ernzerhof exchange–correlation PBE functional. First, we predict the OER energy profiles at different surface metal sites on the $CoMoP_2$ (104) surface (Fig. S10a†) with the clean slab (*) and the surface adsorption species (*OH, *O, and *OOH). On the (104) surface of $CoMoP_2$, the Co and Mo sites form separate stripes containing Co–Co, and Mo–Mo neighbouring pairs, but no Co–Mo pairs. The bridge adsorption at Co–Co and Mo–Mo sites are found to be more favourable than the linear adsorption at a single metal. It appears that Mo is more prone to severe oxidation than Co (Fig. S11a and b†). The predicted OER energy profile suggests that Mo on (104) is naturally hydroxide when no external bias is applied (Fig. S11a†). With an external bias of 1.23 V, bridge Mo_2OH turns into Mo_2O (Fig. S11a†), and no Mo_2OOH or Mo_2OO is formed due to strong Mo–O bonding. In contrast, the bridge Co–Co site exhibits much weaker adsorption for the O and OH species than the Mo–Mo site does, and the formation of Co_2OOH and Co_2OO is viable. The $Co_2O \rightarrow Co_2OOH$ elementary step is the rate-limiting step, with its overpotential predicted to be 0.96 eV. Fig. S11b† also suggests that, without external bias, the Co on (104) is expected to be inhabited by OH species partially and reversibly. At an external bias of 1.23 V, Co on (104) is likely to be covered by OH and O. In addition, the OER on the close-packed (001) surface was also looked into (Fig. S10b and S11c†). Weaker OER activities are found for both Mo and Co site due to too strong adsorption of O species, as compared to the loosely packed (104) surface.

During reaction, the OER occurs simultaneously at many surface sites, which generates partially oxidized catalytic surfaces at any moment. To examine the influences from surface partial oxidation, we probe the OER activity of the Co and Mo sites that are surrounded by hydroxide species (Fig. 5a–d). For OERs at Mo–Mo, the adjacent surface hydroxides do not prevent dissociation of Mo_2OOH resulting in a complete OER cycle (Fig. S11d†). For OERs at Co–Co, the predicted overpotential resulting from the rate-limiting *O → *OOH step is 0.78 eV for the oxidized surface, decreased from 0.96 eV for the clean surface (Fig. S11b†), suggesting that the occupation of the adjacent Co–Co sites by OH enhances the OER activity (Fig. 5e). Such changes are likely due to the "protective" hydroxides attenuating Co's ability to donate electrons to adsorbates (O and OH). The protective OH species at the catalytic Co–Co sites will pull electron densities from the Co sites, and thus slightly increase the oxidation state of Co. As a result, the Co sites are less capable of donating electrons to the OER species at the Co–Co bridge site, as compared to Co on the clean (104) surface with a lower oxidation state. The *O adsorption is more sensitive to the increased oxidation state of Co than the *OH/*OOH adsorption, in terms of adsorption strength, as the former ideally requires an oxidation state change of 2 for Co, whereas the latter only desires an oxidation state change of 1. Therefore, the protective OH prevents the

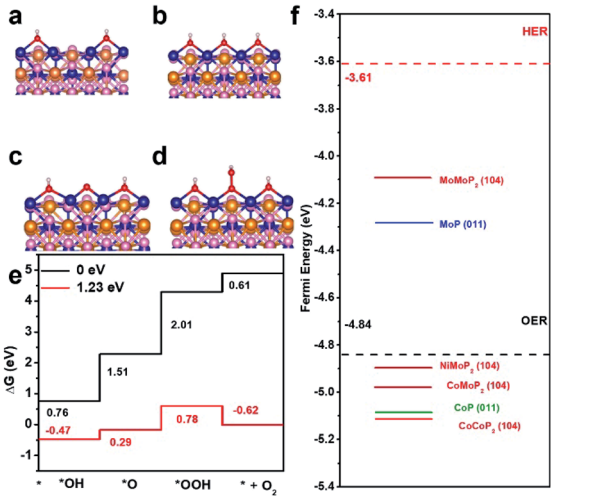

Fig. 5 DFT calculations for the OER over $CoMoP_2$. (a) *, (b) *OH, (c) *O, and (d) *OOH atomistic structures, Co = blue, Mo = orange, P = pink, O = red, H = white. (e) OER free energy profile (Go*) for Co–Co active sites on partially oxidized $CoMoP_2$ (104) surface at the PBE level. (f) Predicted Fermi energies for a range of transition metal phosphates, and colors of the horizontal bars indicate different crystal polymorphs. The vacuum energy is set to zero.

formation of overly stable *O species at the Co–Co bridge, and decreases the Gibbs free energy of reaction for the rate-limiting *O → *OOH step.

We have shown that the surface Co sites are probably the actual catalysts for the OER over $CoMoP_2$, while the hydroxide species are both intermediates and co-catalysts during the OER. Next is to understand the co-catalyzing role Mo plays in the OER. Apparently, Mo is important in defining the crystal symmetry of $CoMoP_2$ (different from those of CoP and MoP) (Fig. S12†). $CoMoP_2$ is essentially a Co-doped MoP with additional inversion symmetry, meaning that the surfaces of $CoMoP_2$ are more alike those of MoP than CoP. In addition, Mo will likely affect the work function of the material, since the work function of Mo and Co metals are ~4.5 and ~5 eV.[61] We calculated the Fermi energies (equivalent to the negative of work function) of the relevant phosphide materials and aligned them with the reduction potentials of HERs and OERs (marked at −3.61 and −4.84 eV for pH = 14), as shown in Fig. 5f. We found that the Fermi levels of $NiMoP_2$ and $CoMoP_2$ (−4.9 and −5.0 eV) are most close to the OER potential (within 0.15 eV), which may favor OERs. A catalyst with the Fermi level far above the OER potential will induce a high surface potential barrier from the electric double layer under OER working conditions, while that far below the OER potential will lose activity due to surface oxidation. Interestingly, the Fermi level of $NiMoP_2$ is the closest to the OER potential among the surveyed systems, showing the strong work-function-tuning effects of Mo. The $NiMoP_2$ (104) surface (Fig. S13†) is predicted to exhibit comparable OER activities as $CoMoP_2$ (104). $NiMoP_2$ is probably a good OER catalyst worth further attention.

Conclusions

In summary, we have developed irregular $CoMoP_2$ nanoparticles consisting of a large number of rough edges under high pressure followed by ball-milling. $CoMoP_2$ nanoparticles exhibit a low overpotential of 270 mV (at 10 mA cm^{-2}) and stable durability in alkaline electrolytes. Our results in both the experiment and the calculation support that the boosting catalytic performance is attributed to the controllable composition, architecture and self-reorganization: (1) unique particle-like shapes consisting of irregular nanoparticles with massive rough edges, which improve the active surface area and the intralayer electron (ion) transfer; (2) self-reconstruction produces highly active Co sites to form a $Co(OH)_2$ layer on the $CoMoP_2$ surface; and (3) Mo atoms regulate the electronic structure facilitating the OER activity. Our results might provide guidance and insights for further design and optimization of the OER catalysts.

Author contributions

S. X., X. G. and A. D. are contributed equally. S. X. fabricated, collected the data, analyzed the data and wrote the paper. X. G. carried out the TEM characterization and analyzed the data. A. D., M. C. and B. W. carried out first-principle calculations and wrote the corresponding section. J. Z. and W. P. performed electrocatalysis measurements. Z. Y. carried out the XPS measurements. N. C. and K. D. F. carried out XAS characterization. Y. G. and F. G. checked the English writing and gave helpful advice. M. W. and M. C. designed the experiments, analyzed the data and was involved in scientific discussions. H. G. designed the experiments, supervised the project and provided financial support.

Conflicts of interest

There are no conflicts to declare.

Acknowledgements

The work was financially supported by National Natural Science Foundation of China (U1930402) and Thousand Youth Talents Program.

Notes and references

1 M. Tahir, L. Pan, F. Idrees, X. Zhang, L. Wang, J. Zou and Z. L. Wang, *Nano Energy*, 2017, **37**, 136–157.
2 C. Han, W. Li, H. K. Liu, S. Dou and J. Wang, *Mater. Horiz.*, 2019, **6**, 1812–1827.
3 H. Wang, J. Wang, Y. Pi, Q. Shao, Y. Tan and X. Huang, *Angew. Chem., Int. Ed.*, 2019, **58**, 2316–2320.
4 H. Sun, X. Xu, Z. Yan, X. Chen, F. Cheng, P. S. Weiss and J. Chen, *Chem. Mater.*, 2017, **29**, 8539–8547.
5 H. Qiu, P. Du, K. Hu, J. Gao, H. Li, P. Liu, T. Ina, K. Ohara, Y. Ito and M. Chen, *Adv. Mater.*, 2019, **31**, 1900843.
6 Y. Yang, L. Dang, M. J. Shearer, H. Sheng, W. Li, J. Chen, P. Xiao and Y. Zhang, *Adv. Energy Mater.*, 2018, **8**, 1703189.
7 P. Mei, J. Kim, N. A. Kumar, M. Pramanik, N. Kobayashi, Y. Sugahara and Y. Yamauchi, *Joule*, 2018, **2**, 2289–2306.
8 J. Xu, X. Wei, J. D. Costa, J. L. Lado, O. B. Baird, L. P. L. Goncalves, S. P. S. Fernandes, M. Heggen, D. Y. Petrovykh and D. R. E. Borkowski, *ACS Catal.*, 2017, **7**, 5450–5455.
9 J. M. Seminario, L. A. Agapito, L. Yan and P. B. Balbuena, *Chem. Phys. Lett.*, 2005, **410**, 275–281.
10 X. Xiao, C. He, S. Zhao, J. Li, W. Lin, Z. Yuan, Q. Zhang, S. Wang, L. Dai and D. Yu, *Energy Environ. Sci.*, 2017, **10**, 893–899.
11 J. Wang and F. Ciucci, *Appl. Catal., B*, 2019, **254**, 292–299.
12 C. Tang, R. Zhang, W. Lu, L. He, X. Jiang, A. M. Asiri and X. Sun, *Adv. Mater.*, 2017, **29**, 1602441.
13 H. Man, C. Tsang, M. M. J. Li, J. Mo, B. Huang, L. Y. S. Lee, Y. Leung, K. Wong and S. C. E. Tsang, *Appl. Catal., B*, 2019, **242**, 186–193.
14 Y. Wang, B. Kong, D. Zhao, H. Wang and C. Selomulya, *Nano Today*, 2017, **15**, 26–55.
15 H. Wan, X. Liu, H. Wang, R. Ma and T. Sasaki, *Nanoscale Horiz.*, 2019, **4**, 789–808.
16 Y. Wu, X. Tao, Y. Qing, H. Xu, F. Yang, S. Luo, C. Tian, M. Liu and X. Lu, *Adv. Mater.*, 2019, **31**, 1900178.
17 Q. Fu, T. Wu, T. Fu, T. Gao, J. Han, Y. Zhang, W. Zhong, X. Wang and B. Song, *ACS Energy Lett.*, 2018, **3**, 1744–1752.

18 X. Hu, S. Zhang, J. Sun, L. Yu, X. Qian, R. Hu, Y. Wang, H. Zhao and J. Zhu, *Nano Energy*, 2019, **56**, 109–117.
19 W. Xu, S. Zhu, Y. Liang, Z. Cui, X. Yang and A. Akihisa, *J. Mater. Chem. A*, 2018, **6**, 5574–5579.
20 G. Li, X. Zhang, H. Zhang, C. Liao and G. Jiang, *Appl. Catal., B*, 2019, **249**, 147–154.
21 L. Zhang, Y. Wang, J. Lv and Y. Ma, *Nat. Rev. Mater.*, 2017, **2**, 17005.
22 J. P. S. Walsh and D. E. Freedman, *Acc. Chem. Res.*, 2018, **51**, 1315–1323.
23 S. D. Kloß, S. Wandelt, A. Weis and W. Schnick, *Angew. Chem., Int. Ed.*, 2018, **57**, 3192–3195.
24 S. Xu, M. Wang, G. Saranya, N. Chen, L. Zhang, Y. He, L. Wu, Y. Gong, Z. Yao, G. Wang, Z. Wang, S. Zhao, H. Tang, M. Chen and H. Gou, *Appl. Catal., B*, 2019, 118385, DOI: 10.1016/j.apcatb.2019.118385.
25 S. Yagi, I. Yamada, H. Tsukasaki, A. Seno, M. Murakami, H. Fujii, H. Chen, N. Umezawa, H. Abe, N. Nishiyama and S. Mori, *Nat. Commun.*, 2015, **6**, 8249.
26 I. Yamada, T. Odake, K. Asai, K. Oka, S. Kawaguchi, K. Wada and S. Yagi, *Mater. Chem. Front.*, 2019, **3**, 1209–1217.
27 H. Sun, X. Jia, L. Deng, P. Lv, X. Guo, Y. Zhang, B. Sun, B. Liu and H. Ma, *J. Mater. Chem. A*, 2015, **3**, 4637–4641.
28 G. Li, C. Fu, J. Wu, J. Rao, S. C. Liou, X. Xu, B. Shao, K. Liu, E. Liu, N. Kumar, X. Liu, M. Fahlman, J. Gooth, G. Auffermann, Y. Sun, C. Felser and B. Zhang, *Appl. Catal., B*, 2019, **254**, 1–6.
29 B. Y. Guan, L. Yu and X. W. Lou, *Angew. Chem., Int. Ed.*, 2017, **56**, 2386–2389.
30 Q. Qin, H. Jang, P. Li, B. Yuan, X. Liu and J. Cho, *Adv. Energy Mater.*, 2019, **9**, 1803312.
31 C. Yuan, S. Zhong, Y. Jiang, Z. Yang, Z. Zhao, S. Zhao, N. Jiang and A. Xu, *J. Mater. Chem. A*, 2017, **5**, 10561.
32 D. Li, H. Baydoun, B. Kulikowski and S. L. Brock, *Chem. Mater.*, 2017, **29**, 3048–3054.
33 Y. Lian, H. Sun, X. Wang, P. Qi, Q. Mu, Y. Chen, J. Ye, X. Zhao, Z. Deng and Y. Peng, *Chem. Sci.*, 2019, **10**, 464–474.
34 L. Hang, Y. Sun, D. Men, S. Liu, Q. Zhao, W. Cai and Y. Li, *J. Mater. Chem. A*, 2017, **5**, 11163–11170.
35 H. Sun, Z. Yan, F. Liu, W. Xu, F. Cheng and J. Chen, *Adv. Mater.*, 2019, 1806326.
36 L. Han, S. Dong and E. Wang, *Adv. Mater.*, 2016, **28**, 9266–9291.
37 C. Wei, R. R. Rao, J. Peng, B. Huang, I. E. L. Stephens, M. Risch, Z. J. Xu and Y. S. Horn, *Adv. Mater.*, 2019, 1806296.
38 P. Zhang, L. Li, D. Nordlund, H. Chen, L. Fan, B. Zhang, X. Sheng, Q. Daniel and L. Sun, *Nat. Commun.*, 2018, **9**, 381.
39 Z. Dai, H. Geng, J. Wang, Y. Luo, B. Li, Y. Zong, J. Yang, Y. Guo, Y. Zheng, X. Wang and Q. Yan, *ACS Nano*, 2017, **11**, 11031–11040.
40 J. Xu, Y. Liu, J. Li, I. Amorim, B. Zhang, D. Xiong, N. Zhang, S. M. Thalluri, J. P. S. Sousa and L. Liu, *J. Mater. Chem. A*, 2018, **6**, 20646–20652.
41 X. Ji, S. Hao, F. Qu, J. Liu, G. Du, A. M. Asiri, L. Chen and X. Sun, *Nanoscale*, 2017, **9**, 7714–7718.
42 Z. Xing, C. Han, D. Wang, Q. Li and X. Yang, *ACS Catal.*, 2017, **7**, 7131–7135.
43 J. A. Koza, C. M. Hull, Y. C. Liu and J. A. Switzer, *Chem. Mater.*, 2013, **25**, 1922–1926.
44 F. Lyu, Y. Bai, Q. Wang, L. Wang, X. Zhang and Y. Yin, *Dalton Trans.*, 2017, **46**, 10545–10548.
45 E. Hu, J. Ning, D. Zhao, C. Xu, Y. Lin, Y. Zhong and Y. Hu, *Small*, 2018, **14**, 1704233; *J. Mater. Sci.*, 2017, **52**, 10406–10417.
46 G. Li, Y. Sun, J. Rao, J. Wu, A. Kumar, Q. N. Xu and X. Feng, *Adv. Energy Mater.*, 2018, **8**, 1801258.
47 B. Liu, H. Li, B. Cao, J. Jiang, R. Gao and J. Zhang, *Adv. Funct. Mater.*, 2018, **28**, 1801527.
48 W. Zhong, M. Liu, J. Dai, J. Yang, L. Mao and D. Yin, *Appl. Catal., B*, 2018, **225**, 180–196.
49 I. Abidat, C. Morais, C. Comminges, C. Canaff, J. Rousseau, N. Guignard and K. B. Kokoh, *J. Mater. Chem. A*, 2017, **5**, 7173–7183.
50 P. F. Liu, X. Li, S. Yang, M. Y. Zu, P. Liu, B. Zhang and H. G. Yang, *ACS Energy Lett.*, 2017, **2**, 2257–2263.
51 M. A. Sayeed, T. Herd and A. P. O'Mullane, *J. Mater. Chem. A*, 2016, **4**, 991–999.
52 Q. Zhang, T. Li, J. Liang, N. Wang, X. Kong, J. Wang, H. Qian, Y. Zhou, F. Liu, C. Wei, Y. Zhao and X. Zhang, *J. Mater. Chem. A*, 2018, **6**, 7509–7516.
53 L. Yu, H. Zhou, J. Sun, I. K. Mishra, D. Luo, F. Yu, Y. Yu, S. Chen and Z. Ren, *J. Mater. Chem. A*, 2018, **6**, 13619–13623.
54 Y. Men, P. Li, J. Zhou, G. Cheng, S. Chen and W. Luo, *ACS Catal.*, 2019, **9**, 3744–3752.
55 D. Jiang, Y. Xu, R. Yang, D. Li, S. Meng and M. Chen, *ACS Sustainable Chem. Eng.*, 2019, **7**, 9309–9317.
56 K. Liu, C. Zhang, Y. Sun, G. Zhang, X. Shen, F. Zou and Y. Zhu, *ACS Nano*, 2018, **121**, 158–167.
57 Y. Lin, Z. Tian, L. Zhang, J. Ma, Z. Jiang, B. J. Deibert, R. Ge and L. Chen, *Nat. Commun.*, 2019, **10**, 162.
58 Q. Li, D. Wang, C. Han, X. Ma, Q. Lu, Z. Xing and X. Yang, *J. Mater. Chem. A*, 2018, **6**, 8233–8237.
59 M. Wang, C. L. Dong, Y. C. Huang and S. Shen, *J. Catal.*, 2019, **371**, 262–269.
60 A. Jain, S. P. Ong, G. Hautier, W. Chen, W. D. Richards, S. Dacek and K. A. Persson, *APL Mater.*, 2013, **1**, 011002.
61 J. Hölzl and F. K. Schulte, *Solid Surface Physics*, 1979, vol. 85, pp. 1–150.